OPTICS

10.1126/sciadv.1500396

Catenary optics for achromatic generation of perfect optical angular momentum

Mingbo Pu,[1]* Xiong Li,[1]* Xiaoliang Ma,[1]* Yanqin Wang,[1] Zeyu Zhao,[1] Changtao Wang,[1] Chenggang Hu,[1] Ping Gao,[1] Cheng Huang,[1] Haoran Ren,[2] Xiangping Li,[2] Fei Qin,[3] Jing Yang,[3] Min Gu,[2] Minghui Hong,[3] Xiangang Luo[1†]

The catenary is the curve that a free-hanging chain assumes under its own weight, and thought to be a "true mathematical and mechanical form" in architecture by Robert Hooke in the 1670s, with nevertheless no significant phenomena observed in optics. We show that the optical catenary can serve as a unique building block of metasurfaces to produce continuous and linear phase shift covering [0, 2π], a mission that is extremely difficult if not impossible for state-of-the-art technology. Via catenary arrays, planar optical devices are designed and experimentally characterized to generate various kinds of beams carrying orbital angular momentum (OAM). These devices can operate in an ultra-broadband spectrum because the anisotropic modes associated with the spin-orbit interaction are almost independent of the incident light frequency. By combining the optical and topological characteristics, our approach would allow the complete control of photons within a single nanometric layer.

INTRODUCTION

As a quantum mechanical description of photons, optical angular momentum is crucial for many classic and quantum applications (*1*). In 1936, Beth first demonstrated that circularly polarized light (CPL) has spin angular momentum of $\pm\hbar$ per photon (*2*). Subsequently, in 1992, Allen and co-workers (*3*) recognized that helically phased beam with $\Phi = l\varphi$ has quantized orbital angular momentum (OAM) of $l\hbar$, where l is known as topological charge. Since then, angular momentum freedom has drawn increasing attention from many realms, including super-resolution imaging (*4*), optical micromanipulation (*5*), optical communications (*6*, *7*), and detection of rotating objects (*8*). Nowadays, light beam carrying OAM can be created by using various optical elements, such as spiral phase plates (*9*), computer-generated holograms (*1*), glued hollow axicons (*10*), form-birefringent elements (*11*, *12*), microscopic ring resonators (*13*), and two-dimensional (2D) nano-antenna arrays (the so-called metasurfaces) (*14*–*19*). In particular, the metasurfaces offer great advantages owing to their low profile and high degree of integration. Owing to the spin-orbit interaction in space-variant anisotropic metasurfaces (*12*, *15*, *19*), CPL can be converted to its cross-polarization state along with the OAM generation, whereas the sign of the OAM is determined by the handedness of the CPL. When the space-variant material is composed of half-wave plates with a rotating optical axis, the CPL can be completely converted (*12*, *15*). However, the thickness of traditional wave plate is often much larger than the operating wavelength as a result of the weak anisotropy (*12*).

Besides these inhomogeneous anisotropic media, it is also well known that chiral structures can interact strongly with CPL and manifest handedness-dependent phase modulation properties (*20*–*25*). The handedness-dependent response of gradient metasurfaces can be considered as one kind of scattering circular dichroism (*26*), owing to the similarity between chirality and spin-orbit interaction. Nevertheless, because of the resonant nature of chiral materials, it is difficult to achieve broadband performance.

In this work, we present a methodology that makes use of metallic structures similar to the natural catenaries to generate a geometrical phase with spatially continuous and spectrally achromatic distribution. The geometric phase is solely determined by the surface structure because it results from the spin-orbit conversion (*12*, *27*) but not the phase accumulation along the optical path (*28*) or impedance transitions (*29*, *30*). On the basis of the unique features of a single catenary, we constructed arrays to generate OAM beams with various kinds of phase distributions. The simultaneous phase control over the azimuthal and radial directions suggests that our strategy is universal for almost arbitrary 2D phase profile.

RESULTS

As shown in Fig. 1A, we describe the optical catenary by the closed area formed by two individual curves with a shift of Δ along the coordinate axis. Such curves are inspired by the spin-orbit interaction in inhomogeneous anisotropic material (*12*) and rigorously derived by integrating the predefined phase function of space-variant shallow gratings (see Supplementary Text and fig. S1). Different from (*12*), the optical catenary does not require the anisotropic material to be a half-wave plate; thus, the thickness could be reduced to tens of nanometers. Owing to the constant phase gradient along the x direction, the corresponding curve might be denoted as "catenary of equal phase gradient" similar with the mechanical "catenary of equal strength," which was first derived in 1826 by Davies Gilbert (*31*)

$$y = \frac{\Lambda}{\pi}\ln(|\sec(\pi x/\Lambda)|) \quad (1)$$

where Λ is the horizontal length of a single catenary. In the catenary (aperture or its complementary structure), the inclination angle between the curve tangent and the x axis, $\xi(x)$, varies from $-\pi/2$ to $\pi/2$ between the left and right endpoints, yielding a linear geometric phase as a result

[1]State Key Laboratory of Optical Technologies on Nano-Fabrication and Micro-Engineering, Institute of Optics and Electronics, Chinese Academy of Sciences, Chengdu 610209, China. [2]Centre for Micro-Photonics and CUDOS (Centre for Ultrahigh Bandwidth Devices for Optical Systems), Faculty of Science, Engineering and Technology, Swinburne University of Technology, P.O. Box 218, Hawthorn, Victoria 3122, Australia. [3]Department of Electrical & Computer Engineering, National University of Singapore, Engineering Drive 3, Singapore 117576, Singapore.
*These authors contributed equally to this work.
†Corresponding author. E-mail: lxg@ioe.ac.cn

of the geometric relation $\Phi(x) = 2\sigma\xi(x)$ (*12*), where $\sigma = \pm 1$ denotes the left- and right-handed circular polarizations (LCP and RCP).

The polarization-dependent geometric phases make the catenary into a compact beam splitter for CPL, which is typically constructed by 3D chiral structures (*32*). It should be noted that the geometric phase in catenary is free of discrete phase sampling as in the case of nano-antenna arrays (*14*). The elimination of discreteness implies that it is possible to move an important step toward the metasurface-assisted law of reflection and refraction (*14*, *33*). Furthermore, the geometric phase in the catenary aperture is intrinsically linear, whereas other deformed shapes, such as crescents and parabolas, are characterized by large-phase nonlinearity, as can be directly calculated using the tangent angles (Fig. 1B).

In principle, owing to the gradient phase distribution, even a single catenary aperture can alter the propagation path of the CPL beam. By arranging the catenaries in various forms, it is possible to obtain an arbitrary phase distribution, such as that featured by spiral phase plates, axicons, and lenses (Fig. 1, C to E). Without the loss of generality, three kinds of phased beams are considered: an ordinary OAM beam, a high-order Bessel beam (HOBB), and a focused beam carrying OAM. The ordinary OAM beam has a spiral phase along the azimuthal direction. The catenary curve in polar coordinates (r and φ) can be derived to represent the corresponding surface topography (see section S1 of the Supplementary Materials for details)

$$r = (r_0 + m\Delta)\left(\left|\sec\left[\frac{(l-2)\varphi}{2}\right]\right|\right)^{\frac{2}{2-l}}, m = 0, 1, 2, 3\ldots \qquad (2)$$

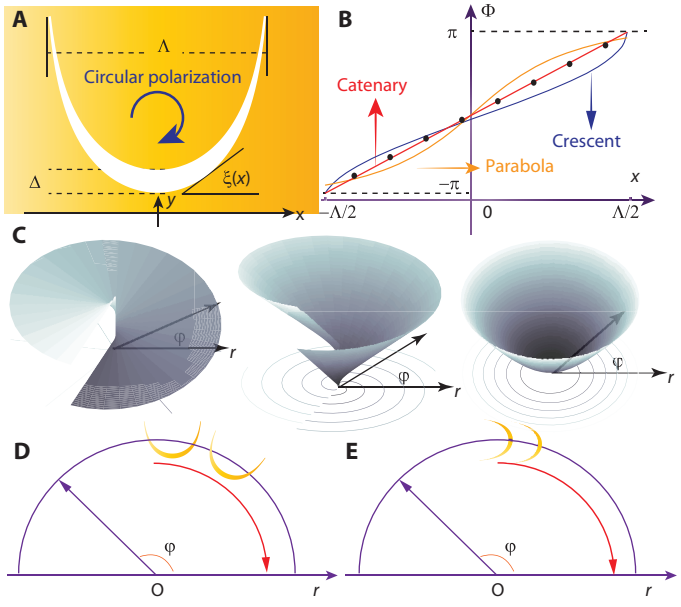

Fig. 1. Schematic representation of the geometric phase in optical catenaries. (**A**) Sketch map of a catenary aperture illuminated at normal incidence by CPL. Light is assumed to propagate along the +*z* direction throughout this paper. The inclination angle with respect to the *x* axis is denoted as $\xi(x)$. (**B**) Phase distributions of the catenary (red), parabola (orange), crescent (blue), and discrete antennas (black dot) for LCP illumination ($\sigma = 1$). (**C**) Three typical kinds of phase profiles for the generation of pure OAM (left), HOBB (middle), and focused beam (right). (**D** and **E**) Arrangement diagrams of the catenary arrays for ordinary OAM (D) and HOBB or focused beam (E).

where r_0 defines the location of the vertex of the innermost curve, Δ is the distance between two vertexes at adjacent curves, and m is the index number of these curves. Following Eq. 2, one can use the catenaries to produce OAM beams with arbitrary topological charge. As an example, a sample with topological charge of $l = -3$ for LCP illumination ($\sigma = 1$, the topological charge is reversed from l to $-l$ for opposite circular polarization) was fabricated via focused ion beam (FIB) milling on a 120-nm-thick gold (Au) film (Fig. 2A), where values of Δ and r_0 are 200 nm and 1.5 μm.

Under CPL illumination, the catenary apertures simultaneously generate two kinds of beams with approximately equal intensity, one uniformly phased and the other helically phased with opposite handedness (second column of Fig. 2A). On the basis of the interference effect, the topological charge of the OAM can be directly identified, without the use

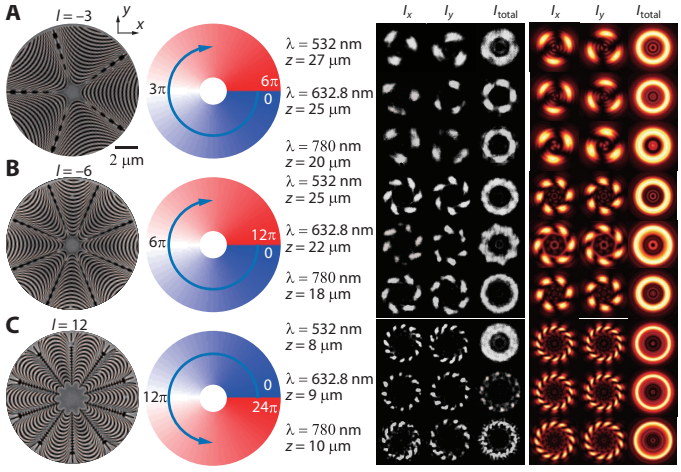

Fig. 2. OAM generators based on catenary arrays. (**A** to **C**) The topological charges for (A) to (C) are −3, −6, and 12 ($\sigma = 1$), respectively. The first column represents the scanning electron microscopy (SEM) images of the fabricated samples. Scale bar, 2 μm. The second column shows the spiral phase profiles. The last two columns depict the measured (the third column) and calculated (the last column) results of I_x, I_y, and I_{total} for λ = 532 nm (top row), 632.8 nm (middle row), and 780 nm (bottom row). The distances between the recording planes and the sample are indicated in each row.

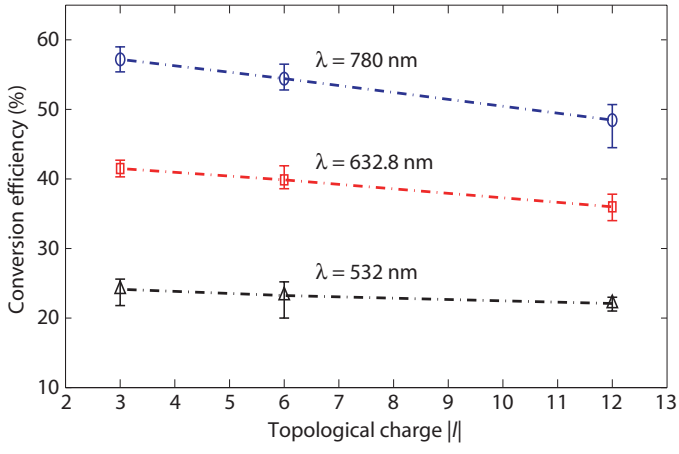

Fig. 3. Measured conversion efficiencies of the OAM generators. Mean values of repeated measurements are given for the samples with $l = -3$, -6, and 12 ($\sigma = 1$) at wavelengths of λ = 532, 632.8, and 780 nm. The error bars give the maximum range of errors.

of additional interference beam (*1*). In the experiment, we adopted three laser sources at λ = 532, 632.8, and 780 nm to investigate the broadband performances. The third column of Fig. 2A represents the intensity patterns for different wavelengths and polarizations, which were recorded at a few micrometers away from the sample and in agreement with the theoretical results obtained by vectorial diffraction theory (see the last column of Fig. 2A) (*34*). For the *x*- and *y*-polarized components, the intensity patterns are manifested by rotating petals encircling the beam centers, where the modulus and sign of *l* are determined by the number and twisting direction of these petals.

To validate the universal applicability of our approach, we fabricated and characterized two additional OAM generators with topological charges of $l = -6$ and 12 ($\sigma = 1$). As we expected, the agreement with theory is good except for some background noise (Fig. 2, B and C). Subsequently, we measured the conversion efficiency η, defined as the ratio of the beam carrying OAM to the overall transmitted power (eq. S8). As depicted in Fig. 3, the mean values for λ = 532, 632.8, and 780 nm are 23.2, 39.8, and 54.4%, exhibiting at least 30-fold enhancement compared with that in circular nanoslits (*16*). In principle, the efficiencies can be further increased by using additional reflective layers

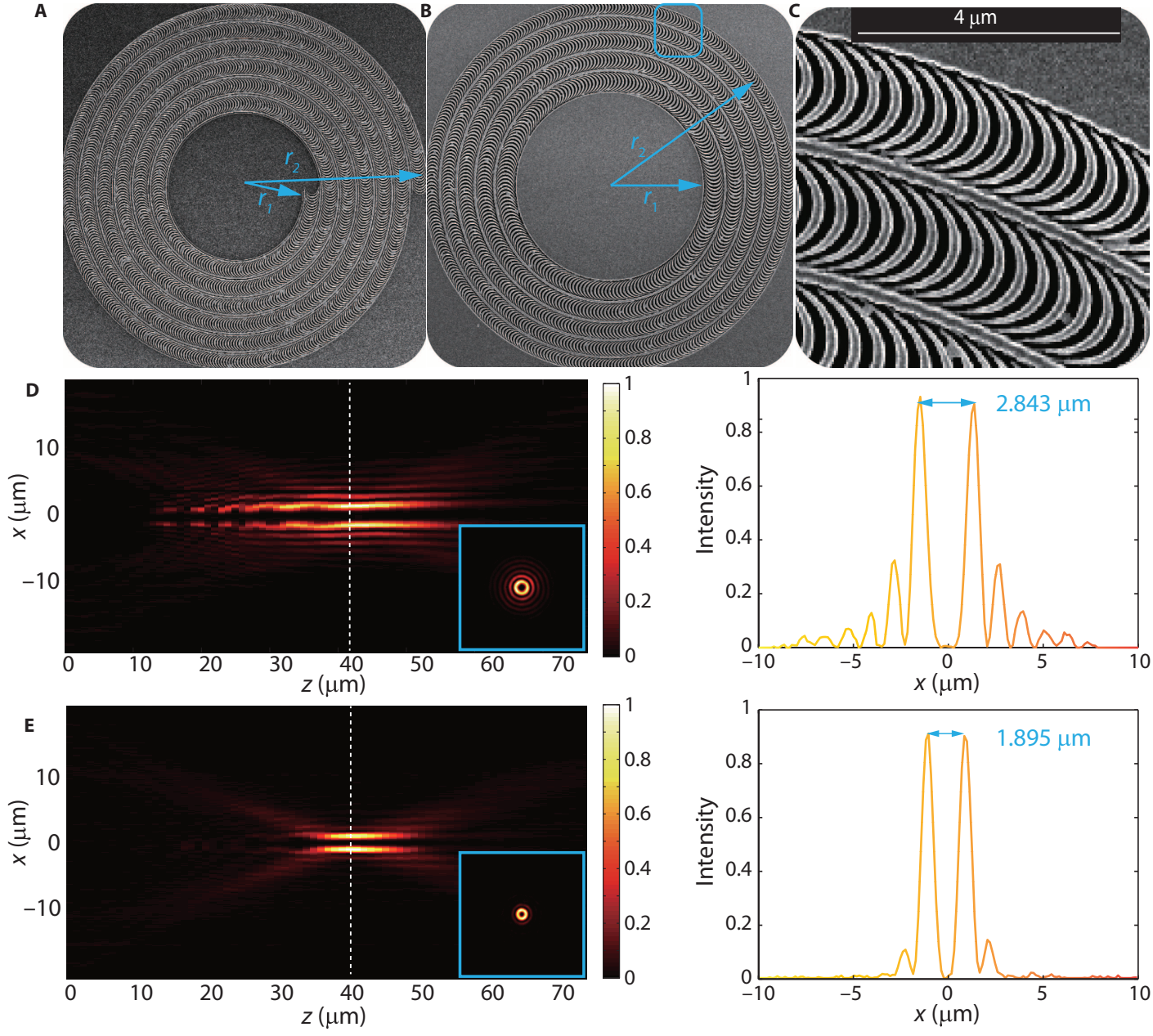

Fig. 4. Catenary arrays for the generation of HOBB and focused OAM beam. (**A** and **B**) SEM images of the catenary arrays for HOBB (A) and focused OAM (B). (**C**) Scaled view of the rectangular region shown in (B). (**D** and **E**) Measured cross-polarized intensity distributions of the HOBB (D) and focused OAM (E) at a wavelength of λ = 632.8 nm for RCP illumination (σ = −1). The intensities at the *xy* plane ($x, y \in [-20, 20]$ μm, $z = 40$ μm) are plotted in the insets.

(*17*, *18*). As an alternative to metallic catenaries, high-index dielectric material can also be used to construct all-dielectric catenaries to enhance the energy efficiency (*15*), although the operating bandwidth would be limited by the resonant nature.

Hereafter, we implement the catenary array to generate the HOBB and focused OAM. The introduction of the Bessel-type radial phase distribution would enable diffraction-free transfer of OAM states, whereas the focused OAM beam has potential application in subdiffraction imaging and micromanipulation. Following the design procedure in fig. S1 (B and C), another two catenary samples were fabricated (Fig. 4, A to C). The predefined phase distributions in the sample plane are as follows

$$\Phi(r\varphi) = \sigma(k_r r + l_1\varphi) \tag{3a}$$

and

$$\Phi(r,\varphi) = \sigma(k\sqrt{r^2+f^2} + l_2\varphi) \tag{3b}$$

where $k = 2\pi/\lambda$ is the wave number in vacuum. The design parameters are $k_r = k{\cdot}\arcsin(\lambda/\Lambda)$, $\Lambda = 2$ μm, $l_1 = 3$, $l_2 = 2$, and $f = 40$ μm. The inner and outer radii, defined as r_1 and r_2, are 7.1 and 20.7 μm for the HOBB generator, and 10.6 and 20.8 μm for the OAM lens. The transmitted intensity patterns at $\lambda = 632.8$ nm were measured using the homebuilt microscopy under RCP illumination ($\sigma = -1$). As shown in Fig. 4D, the intensity distribution along the propagation direction reveals the two main characteristics of the HOBB, that is, the diffraction-free property and the intensity singularity. The intensity map for the planar OAM lens (Fig. 4E), however, is more constrictive along the propagation direction. For the two kinds of devices, the measured center-to-center distances of the doughnut-shaped intensity patterns at $z = 40$ μm are 2.843 and 1.895 μm, which are a bit larger than the theoretically expected 2.54 and 1.56 μm.

CONCLUSION

The most amazing property of the catenary-based OAM generators is their ability to achieve achromatic performance, which can be concluded from the following two observations. On the one hand, the geometric phase is intrinsically independent of the operating frequency according to its definition ($\Phi = 2\sigma\zeta$). On the other hand, the conversion efficiency η is also nearly achromatic, especially when the characteristic dimension is at deep-subwavelength scale. To demonstrate the latter conclusion, the efficiencies for both the catenary apertures and discrete antennas were calculated using commercial software CST Microwave Studio, where the unit cells (cells A and B) were chosen as shown in Fig. 5 (A and B). To increase the accuracy, the measured permittivities for gold and SiO_2 substrates were adopted (*35*) in the numerical simulations. It should be noted that the width w is changing all over the catenary; thus, the period of cell A ($p = 2w$) varies correspondingly (Fig. 5A). As can be seen in Fig. 5C, the efficiencies of cell A for $p = 100$ to 400 nm are depicted in a region shown in gray (the lower envelope of this area corresponds to the lowest efficiency), whereas the results for cell B are evaluated for only $p = 400$ nm. Obviously, the operating bandwidth of the catenary is far beyond that of the discrete antennas, especially in the low-frequency regime. It should be noted that the simulation results obtained from the unit cells represent only an approximation to the real space-variant transmission. Nevertheless, this method provided a simple way to predict the electromagnetic responses, which was widely used in related research (*15*, *17*, *18*).

To explain the physical mechanism of the achromatic η, the electromagnetic modes for the two unit cells are shown in Fig. 5 (D and E). Resorting to the optical nanocircuit theory proposed by Engheta (*36*), we found two orthogonal modes in the catenaries, one inductive and one capacitive, along the main axes. Because the inductive and capacitive modes are related to the achromatic rejection and transmission, one can expect that η is nearly a constant in an ultra-broadband spectrum (see eq. S8). The fluctuation in the visible region is because the unit cell of the catenary has a period close to the operating wavelength; thus, there is an obvious amplitude modulation effect. By treating the catenary as a space-variant grating, we evaluated the transmission coefficients at different locations for both the copolarized and cross-polarized CPL. As shown in fig. S2, both transmission coefficients are dependent on the width of the catenary, and the fluctuation of the copolarized light is a bit larger than its cross-polarized counterpart. At the low-frequency regime, the amplitude modulation effect is much weaker, because the period is in the deep-subwavelength scale and the metals behave more like perfect electric conductors (*14*). As a result, we can expect that if smaller structures are adopted, the amplitude variation can be eliminated.

The periodic change of the amplitudes has two effects: first, for cross-polarized light, the generated field distributions will depart from the ideal case, owing to the additional amplitude modulation; second, for copolarized light, the periodic variation of amplitudes will lead to obvious diffraction. To illustrate these phenomena, we measured the intensity patterns of both the cross-polarized and copolarized compo-

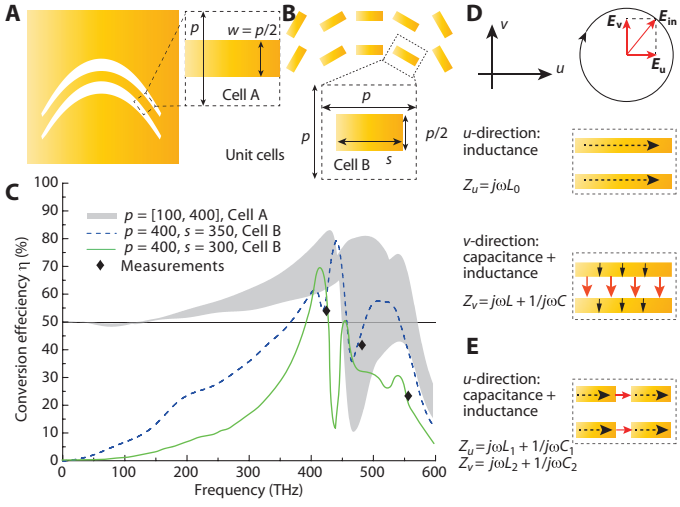

Fig. 5. Comparison of the conversion efficiencies and electromagnetic modes of the catenary apertures and discrete nano-antennas. (**A** and **B**) Schematics of the unit cells in catenary apertures (A, $s = p$) and discrete antennas (B, $s < p$). The two cells differ from each other in the length of the metallic bar with respect to the period. (**C**) Numerically calculated polarization conversion efficiency η for the catenary apertures and nano-antennas. The small discrepancy between the theoretical expectations and the experimental results (Fig. 3) is mainly due to fabrication imperfections. (**D** and **E**) Schematic of the orthogonal modes in the *u*-*v* coordinates for the catenary (D) and discrete antennas (E). The surface impedances as a function of frequency are depicted by the nanocircuit model. The resistances stemming from the ohmic loss are neglected.

nents for a sample designed to generate OAM of $l = \pm 1$. As shown in fig. S3, the cross-polarized intensity departs slightly from the calculated doughnut shape, whereas the copolarized component results in a triangular diffraction pattern (details are discussed in the Supplementary Materials).

In summary, we have theoretically predicted and experimentally demonstrated the intriguing properties of the optical catenaries, which are structures well known in the natural world and widely exploited in architecture but still unfamiliar to optical researchers (*37*, *38*). The perfect OAM demonstrated here, with spatially continuous and spectrally achromatic phase distribution, will allow a revolution of the state-of-the-art techniques with applications such as optical micromanipulation and high-speed photonic communications. As a direct extension of these findings, novel optical functionalities such as giant enhancement of polarization selectivity (*32*) and achromatic light routing (*39*) could be enabled.

MATERIALS AND METHODS

Numerical simulation

The unit cells were simulated using the finite element method in CST Microwave Studio. Two Floquet ports are placed at the $+z$ and $-z$ directions, respectively. The port at the $-z$ direction is attached to the bottom of the SiO_2 substrate, which has a thickness of 1 μm. The distance between the sample surface and the port at the $+z$ direction is also set as 1 μm.

The propagation of the OAM beam was simulated by using vectorial angular spectrum theory (*34*). In all the calculations, we assume that light is propagating along the $+z$ direction. When the electric field distribution at $z = 0$ is known, the vectorial electric field at any plane with $z > 0$ can be written as follows

$$\begin{bmatrix} E_x(x,y,z) \\ E_y(x,y,z) \\ E_z(x,y,z) \end{bmatrix} = \int_{-\infty}^{\infty}\int_{-\infty}^{\infty} \begin{bmatrix} A_{x,z}(m_1,n_1) \\ A_{y,z}(m_1,n_1) \\ \dfrac{m_1 A_{x,z}(m_1,n_1) + n_1 A_{y,z}(m_1,n_1)}{-q} \end{bmatrix} \times \exp(i2\pi(m_1 x + n_1 y))dm_1 dn_1 \quad (4)$$

and

$$\begin{bmatrix} A_{x,z}(m_1,n_1) \\ A_{y,z}(m_1,n_1) \end{bmatrix} = \exp(i2\pi q(m_1,n_1)z) \times \begin{bmatrix} A_{x,z=0}(m_1,n_1) \\ A_{y,z=0}(m_1,n_1) \end{bmatrix}$$

$$= \exp(i2\pi q(m_1,n_1)z)$$

$$\times \int_{-\infty}^{\infty}\int_{-\infty}^{\infty} \begin{bmatrix} E_x(x,y,0) \\ E_y(x,y,0) \end{bmatrix} \times \exp(-i2\pi(m_1 x + n_1 y))dxdy \quad (5)$$

where $m_1 = k_x/2\pi, n_1 = k_y/2\pi, q = \sqrt{1/\lambda^2 - m_1^2 - n_1^2}$ are the spatial frequencies, k_x and k_y are the wave numbers along the x and y directions, $\lambda = \lambda_0/n$ is the wavelength in free space, and n is the refractive index of the background medium.

Sample fabrication

All the samples were fabricated on 1-mm-thick quartz substrates. A 3-nm-thick Cr film and a 120-nm-thick Au film were subsequently deposited on the cleaned substrates by magnetron sputtering in a same sputter chamber. The sputter deposition rates for Cr and Au were $R_{Cr} \approx 0.83$ nm s^{-1} and $R_{Au} \approx 0.92$ nm s^{-1}, respectively. The Cr film was used to improve the adhesion between the Au film and the substrate. Catenary arrays were then milled on the Au/Cr film using a Ga^+ FIB (FEI Helios NanoLab 650), and the accelerating voltage and current of the Ga^+ beam were set as 30 kV and 24 pA, respectively.

Optical setup

All measurements were performed on a homebuilt microscope in transmission mode. First, the incident collimated beam was converted into CPL via the combination of a polarizer and a quarter-wave plate. The transmitted intensity patterns were imaged by using a 60× objective lens and a tube lens, and collected by a silicon-based charge-coupled device (CCD) camera (1600 × 1200 pixels, WinCamD-UCD15, DataRay Inc.). For the measurement of the OAM generators, the interference patterns were filtered by a rotatable polarizer before the CCD camera to obtain the x and y components. For the measurement of copolarized and cross-polarized transmission, a quarter-wave plate and a polarizer were used.

SUPPLEMENTARY MATERIALS

Supplementary material for this article is available at http://advances.sciencemag.org/cgi/content/full/1/9/e1500396/DC1

Text

Fig. S1. Schematic of the integration procedures to design the catenaries.

Fig. S2. Transmission coefficients of the subwavelength grating.

Fig. S3. Design, fabrication, and characterization of the sample with $l = \pm 1$.

REFERENCES AND NOTES

1. S. Franke-Arnold, L. Allen, M. Padgett, Advances in optical angular momentum. *Laser Photonics Rev.* **2**, 299–313 (2008).
2. R. A. Beth, Mechanical detection and measurement of the angular momentum of light. *Phys. Rev.* **50**, 115–125 (1936).
3. L. Allen, M. W. Beijersbergen, R. J. C. Spreeuw, J. P. Woerdman, Orbital angular momentum of light and the transformation of Laguerre-Gaussian laser modes. *Phys. Rev. A* **45**, 8185–8189 (1992).
4. F. Tamburini, G. Anzolin, G. Umbriaco, A. Bianchini, C. Barbieri, Overcoming the Rayleigh criterion limit with optical vortices. *Phys. Rev. Lett.* **97**, 163903 (2006).
5. K. Dholakia, P. Reece, M. Gu, Optical micromanipulation. *Chem. Soc. Rev.* **37**, 42–55 (2008).
6. N. Bozinovic, Y. Yue, Y. Ren, M. Tur, P. Kristensen, H. Huang, A. E. Willner, S. Ramachandran, Terabit-scale orbital angular momentum mode division multiplexing in fibers. *Science* **340**, 1545–1548 (2013).
7. M. Pu, X. Ma, Z. Zhao, X. Li, Y. Wang, H. Gao, C. Hu, P. Gao, C. Wang, X. Luo, Near-field collimation of light carrying orbital angular momentum with bull's-eye-assisted plasmonic coaxial waveguides. *Sci. Rep.* **5**, 12108 (2015).
8. M. P. J. Lavery, F. C. Speirits, S. M. Barnett, M. J. Padgett, Detection of a spinning object using light's orbital angular momentum. *Science* **341**, 537–540 (2013).
9. M. W. Beijersbergen, R. P. C. Coerwinkel, M. Kristensen, J. P. Woerdman, Helical-wavefront laser beams produced with a spiral phaseplate. *Opt. Commun.* **112**, 321–327 (1994).
10. F. Bouchard, H. Mand, M. Mirhosseini, E. Karimi, R. W. Boyd, Achromatic orbital angular momentum generator. *New J. Phys.* **16**, 123006 (2014).
11. G. Biener, A. Niv, V. Kleiner, E. Hasman, Formation of helical beams by use of Pancharatnam-Berry phase optical elements. *Opt. Lett.* **27**, 1875–1877 (2002).
12. L. Marrucci, C. Manzo, D. Paparo, Optical spin-to-orbital angular momentum conversion in inhomogeneous anisotropic media. *Phys. Rev. Lett.* **96**, 163905 (2006).
13. X. Cai, J. Wang, M. J. Strain, B. Johnson-Morris, J. Zhu, M. Sorel, J. L. O'Brien, M. G. Thompson, S. Yu, Integrated compact optical vortex beam emitters. *Science* **338**, 363–366 (2012).
14. N. Yu, P. Genevet, M. A. Kats, F. Aieta, J.-P. Tetienne, F. Capasso, Z. Gaburro, Light propagation with phase discontinuities: Generalized laws of reflection and refraction. *Science* **334**, 333–337 (2011).
15. D. Lin, P. Fan, E. Hasman, M. L. Brongersma, Dielectric gradient metasurface optical elements. *Science* **345**, 298–302 (2014).

16. E. Brasselet, G. Gervinskas, G. Seniutinas, S. Juodkazis, Topological shaping of light by closed-path nanoslits. *Phys. Rev. Lett.* **111**, 193901 (2013).
17. M. Pu, Z. Zhao, Y. Wang, X. Li, X. Ma, C. Hu, C. Wang, C. Huang, X. Luo, Spatially and spectrally engineered spin-orbit interaction for achromatic virtual shaping. *Sci. Rep.* **5**, 9822 (2015).
18. G. Zheng, H. Mühlenbernd, M. Kenney, G. Li, T. Zentgraf, S. Zhang, Metasurface holograms reaching 80% efficiency. *Nat. Nanotechnol.* **10**, 308–312 (2015).
19. X. Ma, M. Pu, X. Li, C. Huang, Y. Wang, W. Pan, B. Zhao, J. Cui, C. Wang, Z. Zhao, X. Luo, A planar chiral meta-surface for optical vortex generation and focusing. *Sci. Rep.* **5**, 10365 (2015).
20. J. K. Gansel, M. Thiel, M. S. Rill, M. Decker, K. Bade, V. Saile, G. von Freymann, S. Linden, M. Wegener, Gold helix photonic metamaterial as broadband circular polarizer. *Science* **325**, 1513–1515 (2009).
21. M. Decker, M. Ruther, C. E. Kriegler, J. Zhou, C. M. Soukoulis, S. Linden, M. Wegener, Strong optical activity from twisted-cross photonic metamaterials. *Opt. Lett.* **34**, 2501–2503 (2009).
22. Y. Zhao, M. A. Belkin, A. Alù, Twisted optical metamaterials for planarized ultrathin broadband circular polarizers. *Nat. Commun.* **3**, 870 (2012).
23. X. Yin, M. Schäferling, B. Metzger, H. Giessen, Interpreting chiral nanophotonic spectra: The plasmonic Born-Kuhn model. *Nano Lett.* **13**, 6238–6243 (2013).
24. Y. Cui, L. Kang, S. Lan, S. Rodrigues, W. Cai, Giant chiral optical response from a twisted-arc metamaterial. *Nano Lett.* **14**, 1021–1025 (2014).
25. X. Ma, C. Huang, M. Pu, C. Hu, Q. Feng, X. Luo, Multi-band circular polarizer using planar spiral metamaterial structure. *Opt. Express* **20**, 16050–16058 (2012).
26. C. Bustamante, I. Tinoco Jr., M. F. Maestre, Circular differential scattering can be an important part of the circular dichroism of macromolecules. *Proc. Natl. Acad. Sci. U.S.A.* **80**, 3568–3572 (1983).
27. K. Y. Bliokh, Y. Gorodetski, V. Kleiner, E. Hasman, Coriolis effect in optics: Unified geometric phase and spin-Hall effect. *Phys. Rev. Lett.* **101**, 030404 (2008).
28. J. Sun, X. Wang, T. Xu, Z. A. Kudyshev, A. N. Cartwright, N. M. Litchinitser, Spinning light on the nanoscale. *Nano Lett.* **14**, 2726–2729 (2014).
29. Q. Feng, M. Pu, C. Hu, X. Luo, Engineering the dispersion of metamaterial surface for broadband infrared absorption. *Opt. Lett.* **37**, 2133–2135 (2012).
30. M. Pu, P. Chen, Y. Wang, Z. Zhao, C. Huang, C. Wang, X. Ma, X. Luo, Anisotropic meta-mirror for achromatic electromagnetic polarization manipulation. *Appl. Phys. Lett.* **102**, 131906 (2013).
31. D. Gilbert, On the mathematical theory of suspension bridges, with tables for facilitating their construction. *Philos. Trans. R. Soc. Lond.* **116**, 202–218 (1826).
32. M. D. Turner, M. Saba, Q. Zhang, B. P. Cumming, G. E. Schröder-Turk, M. Gu, Miniature chiral beamsplitter based on gyroid photonic crystals. *Nat. Photonics* **7**, 801–805 (2013).
33. X. Luo, Principles of electromagnetic waves in metasurfaces. *Sci. China-Phys. Mech. Astron.* **58**, 594201 (2015).
34. A. Ciattoni, B. Crosignani, P. Di Porto, Vectorial free-space optical propagation: A simple approach for generating all-order nonparaxial corrections. *Opt. Commun.* **177**, 9–13 (2000).
35. E. D. Palik, *Handbook of Optical Constants of Solids* (Academic Press, Orlando, FL, 1985).
36. N. Engheta, Circuits with light at nanoscales: Optical nanocircuits inspired by metamaterials. *Science* **317**, 1698–1702 (2007).
37. J. Heyman, Hooke's cubico–parabolical conoid. *Notes Rec. R. Soc. Lond.* **52**, 39–50 (1998).
38. D. J. Coleman, S. K. Fish, Presbyopia, accommodation, and the mature catenary. *Ophthalmology* **108**, 1544–1551 (2001).
39. J. Lin, J. P. B. Mueller, Q. Wang, G. Yuan, N. Antoniou, X.-C. Yuan, F. Capasso, Polarization-controlled tunable directional coupling of surface plasmon polaritons. *Science* **340**, 331–334 (2013).

Acknowledgments: We thank L. L. Yang, H. Zhu, X. C. Lu, and W. B. Xu for their helpful discussions. **Funding:** X. Luo acknowledges the financial support by the 973 Program of China under contract no. 2013CBA01700 and the National Natural Science Funds under contact no. 61138002. M.G. thanks the Australian Research Council for its support (FL100100099 and CE110001018). M.H. acknowledges the CRP project: "National Research Foundation, Prime Minister's Office, Singapore" under its Competitive Research Program (CRP award no. NRF-CRP10-2012-04). **Author contributions:** M.P., Xiong Li, and X.M. contributed equally in the design, fabrication, and characterization of the sample. M.P. and X. Luo wrote the first draft of the manuscript. M.G. and M.H. provided major revisions. All authors discussed the results and commented on the manuscript. X. Luo proposed the original idea and supervised the project. **Competing interests:** The authors declare that they have no competing interests. **Data and materials availability:** All data, analysis details, and material recipes presented in this work are available upon request to X. Luo.

Submitted 27 March 2015
Accepted 17 August 2015
Published 2 October 2015
10.1126/sciadv.1500396

Citation: M. Pu, X. Li, X. Ma, Y. Wang, Z. Zhao, C. Wang, C. Hu, P. Gao, C. Huang, H. Ren, X. Li, F. Qin, J. Yang, M. Gu, M. Hong, X. Luo, Catenary optics for achromatic generation of perfect optical angular momentum. *Sci. Adv.* **1**, e1500396 (2015).

ScienceAdvances

Catenary optics for achromatic generation of perfect optical angular momentum

Mingbo PuXiong LiXiaoliang MaYanqin WangZeyu ZhaoChangtao WangChenggang HuPing GaoCheng HuangHaoran RenXiangping LiFei QinJing YangMin GuMinghui HongXiangang Luo

Sci. Adv., 1 (9), e1500396. • DOI: 10.1126/sciadv.1500396

Science Advances (ISSN 2375-2548) is published by the American Association for the Advancement of Science. 1200 New York Avenue NW, Washington, DC 20005. The title *Science Advances* is a registered trademark of AAAS.